

Characterization of entanglements in glassy polymeric ensembles using the Gaussian linking number

Rasool Ahmad ^{*}, Saptarshi Paul [†] and Sumit Basu [‡]

Department of Mechanical Engineering, Indian Institute of Technology Kanpur, Kanpur 208016, Uttar Pradesh, India



(Received 21 August 2019; accepted 21 January 2020; published 14 February 2020)

We propose a method for enumerating entanglements between long chained, linear polymers that is based on the Gaussian linking number. The linking number is calculated between closely approaching segments of the macromolecular chains. Topological features of an entanglement, i.e., the extent to which one open segment winds around another, are reflected by the linking number. We show that using this measure, we can track disentanglement events through a deformation history and gain insights into how large scale disentanglements lead to failure. Incorporating an additional step where the topological entanglements identified along each chain are optimally clustered using standard clustering algorithms, we can also obtain a measure of the average number of rheological constraints that exist along each chain in an ensemble. Comparisons with other methods of enumerating entanglements, especially the primitive path analysis, are also made. Our results indicate that the linking number between two entangled segments in the undeformed state is a good indicator of the strength of the entanglement. Also, disentanglements occurring overwhelmingly around chain ends are an important cause of failure when a triaxial stress state exists in the polymer.

DOI: [10.1103/PhysRevE.101.022503](https://doi.org/10.1103/PhysRevE.101.022503)

I. INTRODUCTION

Long chains in a polymer melt are known to be entangled. Entanglements are topological constraints on a macromolecular chain, arising out of the basic requirement of the fact that other neighboring chains cannot cross it. Simulations on models of macromolecular chains have shown that it is inevitable that long polymer chains will get entangled and form knots [1]. A successful and complete theory of the viscoelastic properties of polymer melts has been built around the idea that key timescales in the relaxation of a polymer chain are related to the entanglement length N_e (see, e.g., [2]). As shown by Graessley and Edwards [3], entanglement length N_e in a polymer melt can be estimated through the melt plateau modulus G_N^0 of long chained, monodisperse polymers using [4]

$$N_e = \frac{4 \eta k_B T}{5 G_N^0}. \quad (1)$$

Here, ρ is the density and M_0 the molecular weight of a monomer, the constant $\eta = \rho/M_0$. Also, k_B is the Boltzmann constant and T the absolute temperature.

When polymer melts are rapidly quenched to the glassy state, it is widely believed that in the amorphous polymer that forms, the entanglement structure of the melt is closely preserved. In the solid state too, the entanglement structure

plays an important role in determining the deformation and fracture behavior. Most constitutive models (e.g., [5–8]) of glassy, amorphous polymers recognize the importance of entanglements in mechanical behavior, especially in the steep hardening that these materials undergo at large compressive strains. Also, even in the glassy state, where chain mobility is very low, chain pull out resulting from large scale loss of entanglements (or disentanglements) seem to accompany the gradual softening and eventual failure of the material [9,10]. Thus, loss of entanglements (i.e., disentanglements), in addition to chain scission due to highly stretched bonds, is a major cause of failure in glassy polymers. However, it is not clear whether the length relevant to the steep hardening in the glassy state is N_e or shorter (see, e.g., [11,12]).

It is not possible to experimentally determine the length between the topological constraints or entanglements in the glassy state. An alternate strategy can be to construct in the computer, realistic, well equilibrated, atomistically detailed ensembles of a macromolecule and enumerate the entanglements in the ensemble. This has the added advantage that molecular dynamics (MD) simulations can be performed on the ensemble with a view to “observe” how the disentanglement occurs leading to failure. However, to do this, we need a robust strategy to identify entanglements. The task is not trivial and various existing techniques for doing this are described and compared by Hoy *et al.* [13].

For instance, the entanglement network of an ensemble of long chains can be obtained by reducing all chains to their primitive paths (PP), which is the shortest path that a chain fixed at both its ends can follow while respecting the constraint of mutual uncrossability of chains. Sukumaran *et al.* [14] has outlined a procedure by which this can be achieved. This involves (i) fixing all chain ends in a well

^{*}Now at Laboratory for Multiscale Mechanics Modelling, Institute of Mechanical Engineering, EPFL, Lausanne 1015, Switzerland: rasool.ahmad@epfl.ch

[†]sapaul@iitk.ac.in

[‡]Corresponding author: sbasu@iitk.ac.in

equilibrated sample so that their end to end distances remain fixed throughout the subsequent procedures, (ii) turning off all intrachain nonbonded, dihedral, and angle interactions, and (iii) simultaneously reducing the equilibrium bond lengths and the temperature toward zero. Under this procedure, as the ensemble approaches the absolute zero temperature, each chain will tend to straighten out if there are no entanglements. Existence of interchain nonbonded interactions will, however, prevent chain crossings. Thus, the presence of entanglements will reduce each chain to taut piecewise linear curves, with sharp changes in angles or kinks at the location of every entanglement. Once the ensemble has been reduced to a network of PPs, the entanglement length can be calculated by considering the average contour length of the piecewise linear PPs, $\langle L_{PP} \rangle^2$, and the average squared end to end distance $\langle R_{ee}^2 \rangle$. For a chain with N monomers, the entanglement length then is determined using

$$N_e^{\text{rheo}} = (N - 1) \frac{\langle R_{ee}^2 \rangle}{\langle L_{PP} \rangle^2}. \quad (2)$$

The above equation assumes that each PP is a random walk with step lengths N_e^{rheo} .

Alternately, the sharp changes in the direction of the tangent to each chain (treated as a smooth curve in three dimensions) can be tracked to determine the locations of kinks representing entanglement points. In Eq. (2), superscript ‘‘rheo’’ is used to distinguish it from entanglement length obtained by other methods that provide a direct enumeration of entanglements to yield the average number of entanglements per chain $\langle Q \rangle$. Thus,

$$N_e^{\text{topo}} = \frac{N}{\langle Q \rangle}. \quad (3)$$

The topological and rheological measures of entanglement length are not generally identical [9,13,15]. Several other methods exist for determining the topological measure [16–18]. For example, schemes like CReTa [15] and Z1 [16] use a set of geometric operations to iteratively reduce the length of each chain while honoring intersections with other chains. The iterations are carried out until the Euclidean lengths of all chains do not change anymore. The outcome of the exercise is $\langle Q \rangle$, the average number of kinks per chain.

In this work, we attempt to connect the progressive loss of entanglements with large straining of glassy, amorphous polymers with their eventual failure. We have, in earlier works [9,12], tracked the evolution of both topological and rheological entanglement lengths with deformation of a macromolecular sample. Large scale disentanglement at large strains, especially in the presence of large values of stress triaxiality (i.e., the ratio between the mean and equivalent stress at a point is large, as would occur, e.g., when a tensile stress is superposed on a purely hydrostatic stress), is a reason for the loss of stress carrying capacity and eventual failure in amorphous, glassy polymers (see also [10]). Regions of high triaxiality occur, for example, ahead of sharp cracks.

To this end, note the following:

(1) We propose a method for enumerating entanglements in amorphous glassy polymeric samples, that yield a measure for N_e^{topo} . We also show that incorporating an additional step

involving clustering of the topological entanglement points (using standard clustering algorithms) along every chain will also yield a measure of N_e^{rheo} .

(2) Further, we use the developed method to track the loss of entanglements in samples that are imparted large deformations with varying degrees of stress triaxiality. This is done to understand the interplay between the linking number of an entanglement, its propensity for disentanglement, and the imposed stress state at a point in the material.

Use of linking number to characterize the entanglement structure of open macromolecules has received attention in recent years (e.g., a review of recent results, open questions, and applications is available [19]; an early application of knot theory to open random walks can be found in [20]). Writhe and linking number together have been shown to characterize entanglements in linear polymers [21–23].

We use a method that is similar in spirit, though different in implementation, to that proposed by Panagiotou *et al.* [21]. We had proposed a preliminary version of our method in Venkatesan and Basu [10]. Here, a more robust computational implementation is described.

Topological entanglements are identified by our method as a postprocessing exercise from a well equilibrated sample of long chained macromolecules with the current coordinates of each monomer as the only input. The scheme is quick and noniterative. This is especially useful in situations where we are studying the evolution of the entanglement network with deformation. In fact, we further show that, using this measure of N_e^{topo} , we can gain important insights into the nature of imposed deformation required to cause failure by large scale disentanglements and the manner in which these disentanglements occur as deformation proceeds.

In particular, we propose a fast and simple algorithm for computing the linking number between two segments of predetermined length, in two different chains, to detect entanglements. At the moment, the method is suited for ensembles containing only linear polymers.

The concept of linking number between ring polymers has a firm mathematical basis in the sense that the linking number between two closed curves is a topologically invariant integer. Two closed curves cannot disentangle unless crossing is allowed. The invariants can be computed by various established methods like counting of crossings in a link diagram or use of knot polynomials like Alexander, Jones, or HOMFLY. Qin and Milner [24] have predicted entanglement lengths in ring polymers in melts by studying their topological states using the Jones polynomial. Linking in ring polymers has also been studied by Ferrari *et al.* [25] and Tubiana *et al.* [26].

A pair of linear chains, unlike rings, can always be unlinked by sliding one along the length of the other. Yet, the idea of using the linking number to characterize entanglements in ensembles of long linear macromolecules has been explored by a number of authors. The occurrence of knots in long polymer molecules has been recognized way back in the 1960s by Frisch and Wasserman [27] and Delbrück [28]. Sumners and Whittington [1] had shown that as random walks on three-dimensional cubic lattices become long, they inevitably form knots. Panagiotou *et al.* [29] have further shown that two polymers modeled as oriented random walks of length n in a confined volume have mean squared linking number of

the order of n^2 . The concept of the linking number between open curves has been used to characterize entanglements in more detailed macromolecular models. Mansfield [30] used the Alexander polynomial to characterize the knotting of a long protein molecule with itself and concluded that proteins seem to fold in a manner as to avoid knotted configurations. A systematic study of the ensemble averaged linking number in an dense polymer melt has been conducted by Orlandini *et al.* [31]. In their computational scheme, they divided the ensemble of long chain polymers into small cubes and studied the linking number between subchains in each cube in an effort to quantify the entanglement complexity. For modest values of monomer density, the averaged linking number seems to scale as $L^{4/3}$, where L is the size of the cube used. In an earlier work [10], we have used a similar algorithm to compute the linking number between chain segments in a glassy polymeric system. We also followed the evolution of the entanglements over the deformation history of the ensemble. Further advances in methods of detecting and classifying entanglements between open chains using the concept of the linking number have been reported in a recent paper by Caraglio *et al.* [32]. Viscoelastic properties of polymers have been connected to the mean absolute writhe by [23].

In this work, the Gaussian linking number is used to detect entanglements between segments of long chains. The computation of the Gaussian linking number has been done using an efficient technique given by Klenin and Langowski [33]. Mobility of macromolecular chains is low in the glassy state and linking number between segments change with deformation only very close to failure, where large scale disentanglements occur in order to effect pullout of chains at the fracture surface. We have studied the mechanism of disentanglement during deformation by tracking the evolution of linking numbers between segments with deformation.

In the next section, the algorithms used for computing the Gaussian linking number are discussed. The general behavior of the Gaussian linking number, when applied to open curves, is briefly discussed. Possible connections between experimentally measured entanglement length N_e and the Gaussian linking number are also explored in the same Sec. II, along with comparison between our estimates of N_e and those obtained by other methods (especially methods like PP which involve shrinking of chains). Evolution of the entanglement network with different modes of deformation is discussed in Sec. III. Salient conclusions are given in Sec. IV.

II. COMPUTATIONAL DETAILS

A. Preparation and equilibration of samples of long chained polymers for MD simulations

The atomistic sample used in this work comprises 160 macromolecular chains with 1000 united atoms per chain. The process of preparing a well equilibrated, mechanically isotropic sample at a temperature well below the glass transition temperature is described in detail in Mahajan and Basu [11]. Exactly the same procedure is followed here. Moreover, following Mahajan and Basu [11], we have ensured that all targets indicating proper equilibration are met by the sample.

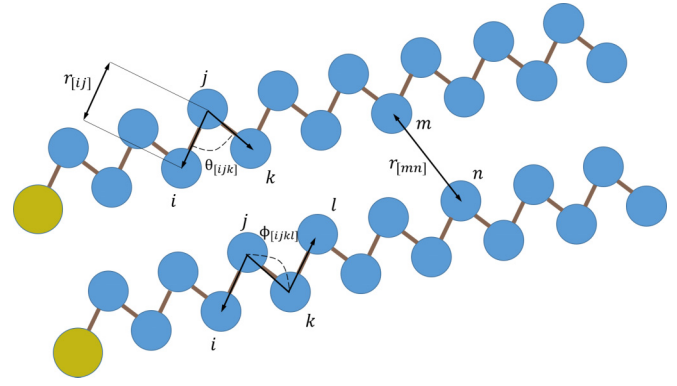


FIG. 1. Notation used in this work to label united atoms, bonds, bending, dihedral angles, and nonbonded interactions.

We use a detailed atomistic model of the polymer for which the total internal energy is given by

$$E = \sum_{[ij]=1}^{n_b} E_b(r_{[ij]}) + \sum_{[ijk]=1}^{n_\theta} E_\theta(\theta_{[ijk]}) + \sum_{[ijkl]=1}^{n_\phi} E_\phi(\phi_{[ijkl]}) + \sum_{[mnl]=1}^{n_{nb}} E_{nb}(r_{[mnl]}). \quad (4)$$

In our notation, explained in Fig. 1, $r_{[ij]}$ denotes the distance between a generic pair of consecutive intrachain united atoms i and j forming a bond. Also, n_b is the total number of bonds in the sample. Similarly, n_θ and n_ϕ stand for total number of bond and dihedral angles while $[ijk]$ and $[ijkl]$ are generic sets of three and four consecutive intrachain atom indices that form a bond angle and a dihedral angle, respectively. In the same way, the number of generic nonbonded pairs $[mnl]$ of united atoms is denoted by n_{nb} where m and n can be located on different chains or be a nonbonded pair of united atoms in the same chain.

Although we do not aim to simulate a particular type of polymer, the coarse grained force field used in this work closely resembles that for polyethylene (PE) given in Fukuda and Kuwajima [34]. The end united atoms of the polymer chain represent CH_3 while other united atoms within the polymer chain represent CH_2 .

The force field consists of following types of potentials:

(1) A harmonic bond stretching potential between two consecutive atoms i and j of the same chain:

$$E_b(r_{[ij]}) = \frac{1}{2}k_b(r_{[ij]} - r_0)^2, \quad (5)$$

where k_b is bond stiffness r_0 is equilibrium value of the bond length $r_{[ij]}$.

(2) A bending potential harmonic about equilibrium bond angle θ_0 :

$$E_\theta(\theta_{[ijk]}) = \frac{1}{2}k_\theta[\cos(\theta_{[ijk]}) - \cos(\theta_0)]^2, \quad (6)$$

where k_θ is bending stiffness and θ_0 the equilibrium value of the bond angle $\theta_{[ijk]}$.

(3) A dihedral potential of the form

$$E_\phi(\phi_{[ijkl]}) = \frac{1}{2}\{A_1[1 + \cos(\phi_{[ijkl]})] + A_2[1 - \cos(2\phi_{[ijkl]})] + A_3[1 + \cos(3\phi_{[ijkl]})]\}, \quad (7)$$

TABLE I. Functional form and parameters of force field.

Type of potential	Functional form	Parameter values
Bond stretching	$E_b = \frac{1}{2}k_b(r_{[ij]} - r_0)^2$	$k_b = 2745 \text{ kJ } \text{\AA}^{-2} \text{ mol}^{-1}$ $r_0 = 1.53 \text{ \AA}$
Angle bending	$E_\theta = \frac{1}{2}k_\theta(\theta_{[ijk]} - \theta_0)^2$	$k_\theta = 749 \text{ kJ mol}^{-1}$ $\theta_0 = 113^\circ$
Dihedral	$E_\phi = \frac{1}{2}[A_1(1 + \cos \phi_{[ijkl]}) + A_2(1 + \cos 2\phi_{[ijkl]}) + A_3(1 + \cos 3\phi_{[ijkl]})]$	$A_1 = 7.86 \text{ kJ mol}^{-1}$ $A_2 = -4.36 \text{ kJ mol}^{-1}$ $A_3 = 15.56 \text{ kJ mol}^{-1}$ Between CH ₃
Nonbonded	$E_{nb} = 4\epsilon\left[\left(\frac{\sigma}{r_{[mn]}}\right)^{12} - \left(\frac{\sigma}{r_{[mn]}}\right)^6\right]$	$\sigma = 3.76 \text{ \AA}$ $\epsilon = 0.88 \text{ kJ mol}$ Between CH ₂ $\sigma = 4.06 \text{ \AA}$ $\epsilon = 0.36 \text{ kJ mol}$

where A_1 , A_2 , A_3 , and A_4 are constants and $\phi_{[ijkl]}$ denotes the dihedral angle formed by atoms with indices i , j , k , and l .

(4) A nonbonded Lennard Jones (LJ) potential of the form

$$E_{nb}(r_{mn}) = 4\epsilon \left\{ \frac{\sigma^{12}}{r_{[mn]}^{12}} - \frac{\sigma^6}{r_{[mn]}^6} \right\}, \quad (8)$$

where ϵ is depth of LJ potential well at $r_{[mn]} = 2^{1/6}\sigma$ and σ is finite distance between interacting atoms at which the LJ potential becomes zero.

Values of all parameters of force field used in this work are taken from Fukuda and Kuwajima [34] and are summarized in Table I.

All simulations are performed with the parallel molecular dynamics code LAMMPS [35] at 100 K, which is well below the glass transition temperature for this case (the glass transition temperature for this sample is between 230 and 240 K (see [11])). All NVT simulations are performed using a Nosé-Hoover thermostat and all NPT simulations additionally use a Nosé-Hoover barostat. Integration of the Newtonian equations of motion is carried out using the velocity Verlet algorithm with time step of $\Delta t = 1$ fs. Periodic boundary conditions are used in all directions. The macromolecular ensemble studied in this work comprises 160 000 united atoms.

The stress measure used in this work is the virial stress [36], the component $\sigma_{\alpha\beta}$ ($\alpha, \beta \in [1, 3]$) of which for the chosen force field is calculated over the ensemble volume V as

$$\begin{aligned} V\sigma_{\alpha\beta} = & -\frac{1}{2} \sum_{[mn]=1}^{n_{nb}} \left\{ r_{m\alpha} \frac{\partial E_{nb}(r_{[mn]})}{\partial r_{m\beta}} + r_{n\alpha} \frac{\partial E_{nb}(r_{[mn]})}{\partial r_{n\beta}} \right\} \\ & -\frac{1}{2} \sum_{[ij]=1}^{n_b} \left\{ r_{i\alpha} \frac{\partial E_b(r_{[ij]})}{\partial r_{i\beta}} + r_{j\alpha} \frac{\partial E_b(r_{[ij]})}{\partial r_{j\beta}} \right\} \\ & -\frac{1}{3} \sum_{[ijk]=1}^{n_\theta} \left\{ r_{i\alpha} \frac{\partial E_\theta(\theta_{[ijk]})}{\partial r_{i\beta}} + r_{j\alpha} \frac{\partial E_\theta(\theta_{[ijk]})}{\partial r_{j\beta}} \right. \\ & \left. + r_{k\alpha} \frac{\partial E_\theta(\theta_{[ijk]})}{\partial r_{k\beta}} \right\} \end{aligned}$$

$$\begin{aligned} & -\frac{1}{4} \sum_{[ijkl]=1}^{n_\phi} \left\{ r_{i\alpha} \frac{\partial E_\phi(\phi_{[ijkl]})}{\partial r_{i\beta}} + r_{j\alpha} \frac{\partial E_\phi(\phi_{[ijkl]})}{\partial r_{j\beta}} \right. \\ & \left. + r_{k\alpha} \frac{\partial E_\phi(\phi_{[ijkl]})}{\partial r_{k\beta}} + r_{l\alpha} \frac{\partial E_\phi(\phi_{[ijkl]})}{\partial r_{l\beta}} \right\} - \sum_{k=1}^{n_{atom}} m v_{k\alpha} v_{k\beta}, \end{aligned}$$

where terms on the right in parentheses represent the contributions to the stress $\sigma_{\alpha\beta}$ from nonbonded, bond stretching, bond bending, dihedral interaction, and kinetic energy, respectively. Other microscopic stress definitions for molecular system can be found in Admal and Tadmor [37].

B. Deformation fields imposed on the samples

The sample generated by the procedure outlined in the previous section is subjected to four simple deformation fields. In each case, entanglements are identified at various stages of the deformation. Individual entanglements are followed throughout the deformation history and disentanglements are tracked. The deformation fields imposed on the atomistic sample are shown in Fig. 2.

The initial sample has dimensions $L_1 = L_2 = 95$ and $L_3 = 476$ Å in the e_α ($\alpha \in [1, 3]$) coordinate system. At any point of time t , the dimensions of the sample are denoted by l_α . Coordinate points in space in the reference configuration at time $t = 0$ are denoted by X_α , while coordinates of the united atom I in the reference configuration are denoted by $X_{\alpha I}$. Similarly, coordinate points in subsequent configurations are denoted by $x_\alpha(t)$ and united atom coordinates by $x_{\alpha I}$. Velocities are denoted by $v_\alpha(\mathbf{x}, t)$ and $v_{\alpha I}(\mathbf{x}, t)$ for points in space and united atom I .

The following deformation fields are imposed:

(1) Uniaxial stretching with imposed hydrostatic stress is generated by stretching the sample at constant velocity in the 3 direction while keeping the dimensions in the other two directions fixed. Thus,

$$\begin{aligned} v_1(l_1, x_2, x_3, t) &= v_1(0, x_2, x_3, t) \\ &= v_2(x_1, l_2, x_3, t) = v_2(x_1, 0, x_3, t) \\ &= v_3(x_1, x_2, 0, t) = 0, \end{aligned} \quad (9)$$

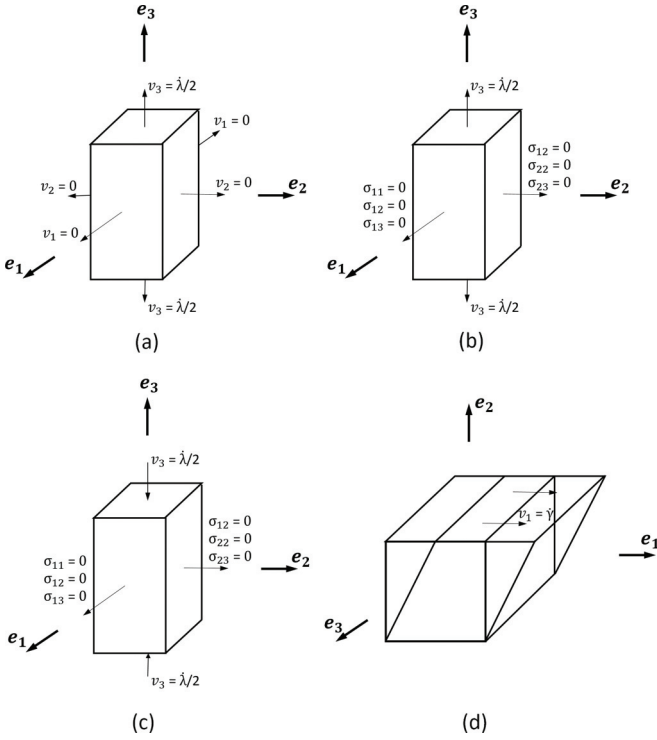


FIG. 2. Coordinate systems and boundary conditions applied during (a) uniaxial stretching under high hydrostatic stress, (b) pure uniaxial stretching, (c) uniaxial compression, and (d) simple shear.

while $v_3(x_1, x_2, l_3) = \dot{\lambda}$, where $\dot{\lambda}$ is a constant. At a point of time t , the total stretch in the 3 direction is λ .

(2) Pure uniaxial tension and compression are performed in $N\sigma_{11}\sigma_{22}T$ ensemble where $\sigma_{11} = \sigma_{22} = 0$ at all t . Further, we impose

$$v_3(x_1, x_2, l_3, t) = \pm \dot{\Gamma}, \quad (10)$$

with the positive sign for tension and the negative for compression.

(3) Finally, a simple shear deformation is imparted by imposing

$$v_1(x_1, x_2, 0, t) = v_2(x_1, x_2, 0, t) = v_3(x_1, x_2, 0, t) = 0 \quad (11)$$

and

$$v_1(x_1, x_2, l_3, t) = \dot{\gamma}, \quad (12)$$

so that the engineering shear strain γ_{12} at any time t is given as

$$\Gamma = \frac{\dot{\gamma}t}{L_2}. \quad (13)$$

C. Linking number and its computation

We use the linking number to identify and characterize entanglements between polymer chains. As mentioned earlier, the linking number is a topological invariant for two closed and linked curves. For such cases, a simple method can be used to determine the linking number. This involves projecting the link diagram of the two closed curves onto an arbitrary plane keeping the information of overpassing and underpassing at crossings intact. Each crossing point is assigned +1 or

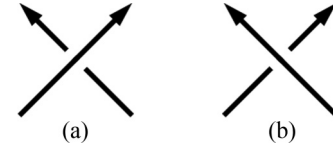


FIG. 3. Types of crossings resembling (a) are assigned +1 and (b) are assigned -1.

-1 depending on the type of crossing shown in Fig. 3. If c_i is the sign assigned to i th crossing in the projection of the linking diagram, the linking number of the two closed chains is given by

$$Lk = \frac{1}{2} \sum_i c_i. \quad (14)$$

If this method is to be used for open chains, a closing scheme needs to be devised as done in Venkatesan and Basu [10] and Caraglio *et al.* [32]. The linking number in this case may depend on the closing scheme. We use the Gaussian linking number that does not need a closing scheme for its calculation. As a result, we obtain a fractional value of the linking number, which is not an invariant as in the case of closed links.

Gaussian linking number

The Gaussian linking number between two curves C_1 and C_2 was defined by Gauss [38]. Originally, this number arose from Gauss' investigations into electromagnetic theory and represented the line integral of the magnetic field induced in C_2 by a current flowing through C_1 [39], i.e.,

$$Lk_G(C_1, C_2) = \frac{1}{4\pi} \int_{C_1} \int_{C_2} (d\mathbf{r}_1 \times d\mathbf{r}_2) \cdot \frac{\mathbf{r}_2 - \mathbf{r}_1}{|\mathbf{r}_2 - \mathbf{r}_1|^3}, \quad (15)$$

where \mathbf{r}_i denotes a point on the curve C_i .

This function from Eq. (15) yields an integer number [which equals that obtained from Eq. (14)] for two linked closed curves C_1 and C_2 .

It has been shown by Klenin and Langowski [33] and Arai [40] that the integrals in Eq. (15) can be computed as

$$Lk_G(C_1, C_2) = \frac{1}{4\pi} \int_{C_1} \int_{C_2} d\Omega(\mathbf{r}_1, \mathbf{r}_2). \quad (16)$$

Here, $d\Omega$ is a signed solid angle. In Fig. 4(b),

$$d\Omega_{12}^* = \frac{|(d\mathbf{r}_1 \times d\mathbf{r}_2) \cdot \mathbf{r}_{12}|}{|\mathbf{r}_{12}|^3} \quad (17)$$

is the solid angle formed by $d\mathbf{A} = d\mathbf{r}_1 \times d\mathbf{r}_2$ and \mathbf{r}_{12} at \mathbf{A} . The signed solid angle $d\Omega(\mathbf{r}_1, \mathbf{r}_2)$ equals $d\Omega_{12}^*$ if the crossing of vectors $d\mathbf{r}_1$ and $d\mathbf{r}_2$ is right handed and $d\Omega(\mathbf{r}_1, \mathbf{r}_2) = -d\Omega_{12}^*$ if it is left handed.

In the case of two curves each composed of N piecewise straight segments, Eq. (16) can be expressed as the double sum

$$Lk_G(C_1, C_2) = \frac{1}{4\pi} \sum_{I=1}^N \sum_{J=1}^N \Omega_{IJ}, \quad (18)$$

where Ω_{IJ} is the solid angle formed by all those projections in which a pair of segments I and J appear to cross each other. Thus, for two straight segments $I, I+1$ and $J, J+1$ [shown

in Fig. 5(a)], the solid angle Ω_{IJ} is formed by vectors $k, l, m,$ and n , as shown in Fig. 5(b). To compute solid angle, we make use of equality obtained by Van Oosterom and Strackee [41],

$$\Omega(k, l, m) = 2 \arctan \left(\frac{[k, l, m]}{|k||l||m| + (k \cdot l)|m| + (m \cdot k)|l| + (l \cdot m)|k|} \right), \tag{19}$$

where $[k, l, m]$ is the scalar triple product of vectors $k, l,$ and $m,$ and $|k|$ is norm of vector $k.$ Hence, the solid angle made by all those views in which two segments $(I, I + 1)$ and $(J, J + 1)$ apparently cross is

$$\Omega_{IJ} = 2 \left[\arctan \left(\frac{[k, l, m]}{|k||l||m| + (k \cdot l)|m| + (m \cdot k)|l| + (l \cdot m)|k|} \right) + \arctan \left(\frac{[m, n, k]}{|m||n||k| + (m \cdot n)|k| + (k \cdot m)|n| + (n \cdot k)|m|} \right) \right]. \tag{20}$$

We compute Gaussian linking number by using Eqs. (18) and (20).

A few features of the measure $Lk_G(C_1, C_2)$ for open curves C_1 and $C_2,$ can be illustrated by taking C_1 as a vertical straight segment around which C_2 winds helically [see Figs. 6(b)–6(d)]. Two closed curves, as shown in Fig. 6(a), where C_2 executes n full turns around $C_1,$ has a linking number of $n.$ In Fig. 6(a), the linking number is 5. If C_1 is open but vertical and long, as in Fig. 6(b), Lk_G for n complete turns of C_2 lies between n and $n + 1.$ The fractional increase in the linking number arises out of the incomplete turns at the beginning and end of the helix C_2 [shown in white in Fig. 6(b)].

that gives the solid angle of a triangular pyramid bounded by three vectors $k, l,$ and $m.$ The solid angle $\Omega(k, l, m)$ is calculated as

The case where C_2 executes incomplete windings around C_1 is important to understand. In this case, the length of C_1 and the radius of C_2 both play a role in determining $Lk_G.$ Thus, in the case shown in Fig. 6(c), the linking number is close to unity only when C_1 is long enough and the radius of C_2 is small. When the radius increases making the pair easier to separate, the linking number falls below unity, even though C_2 executes one full turn. The linking number also falls below 1 also when C_1 is too short implying that C_2 can slide along C_1

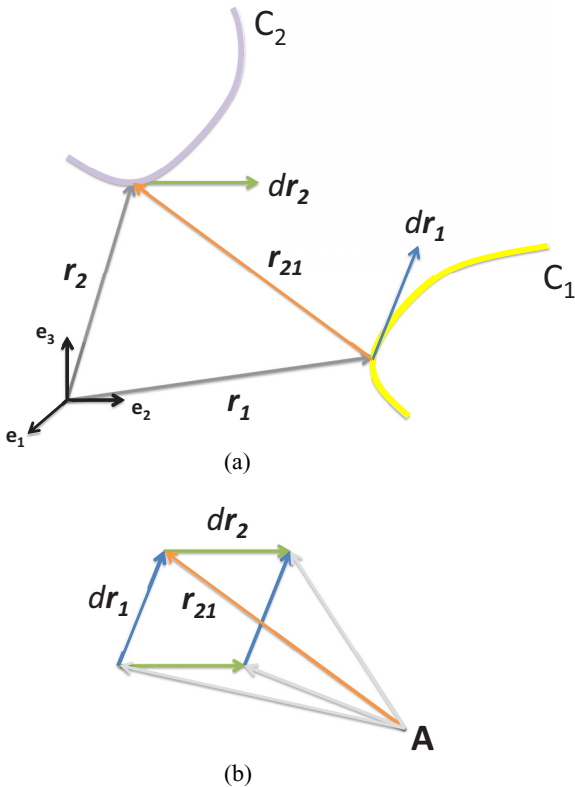


FIG. 4. Quantities pertaining to the two curves C_1 and $C_2,$ used in Eq. (15) are shown in (a). The solid angle $d\Omega_{12}^*$ formed by $dr_1, dr_2,$ and r_{21} at **A** is shown in (b).

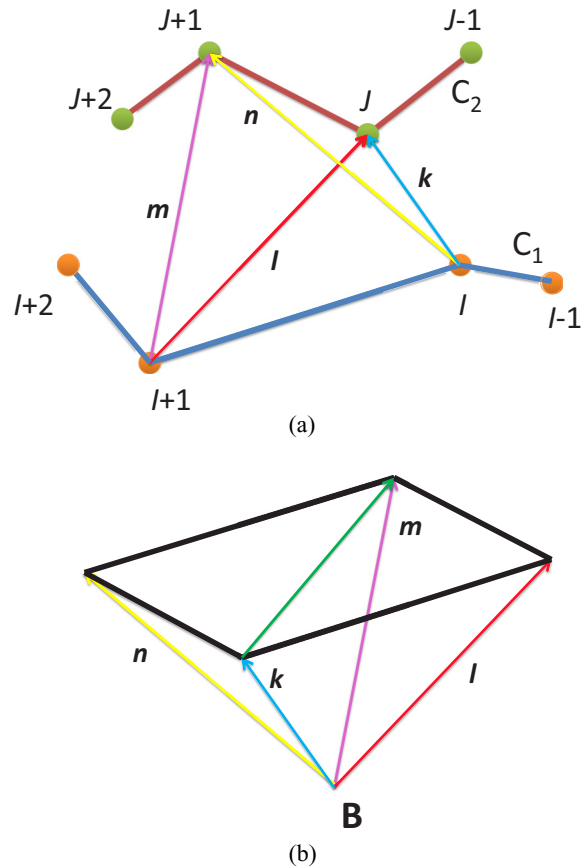


FIG. 5. Calculation of the solid angle Ω_{IJ} between segments I and $J,$ bounded by $I, I + 1$ and $J, J + 1,$ respectively, involves the vectors $k, m, n,$ and l shown in (a). The solid angle Ω_{IJ} formed at **B** in (b) is calculated using $\Omega(k, l, m)$ and $\Omega(k, m, n)$ as in Eq. (20).

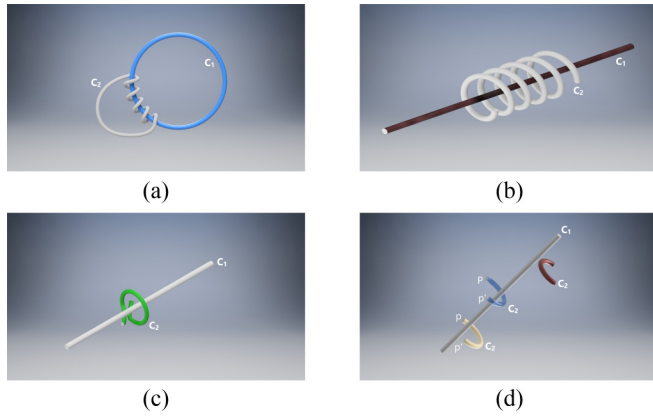


FIG. 6. For two closed curves C_1 and C_2 in (a), the linking number is 5. For open curves as in (b), (c) and (d), the linking number is nonintegral. It is 4.8 in (b), 0.9 in (c) and 0, 0.7, and 0.4 (top to bottom, respectively) for the cases shown in (d).

and escape through the ends. Thus, fractional linking numbers between two open curves may imply that one or both curves are short or they are loosely linked. In either case, low linking number indicates that unlinking is easier.

Linking numbers less than 1 in fact can serve as an index of “separability” of the curves. Three chains around C_1 are shown in Fig. 6(d). In all the cases the length of C_2 is fixed and it executes an incomplete turn around C_1 . In the topmost case, the linking number is evidently zero as the curves can be pulled away from each other without crossing. In case of the curve in the middle, the angle subtended by C_2 on C_1 is large, implying a tighter winding and the linking number is >0.5 . For the case shown at the bottom, C_2 , the linking number is <0.5 . In all these cases the curve C_2 can be unlinked from C_1 without crossing it or without having to slide C_2 along C_1 . It is obvious for the topmost case. In the other two, since incomplete turns around C_1 are involved, one can envisage a disentangling mechanism where C_1 escapes through the gap PP' shown.

In summary, fractional linking number between two curves indicates that one curve winds around another but executes less than a full turn. The lower the linking number goes below 1, the looser is the entanglement between them. In this paper, we take two segments of different polymer chains to be unentangled when $Lk_G < 0.4$.

D. Identification of entanglement network

In order to identify the entanglement network using Lk_G between neighboring segments, we need to start with the position vectors \mathbf{x}_I of all atoms I in the ensemble. The problem of calculating linking numbers between chains in a periodic system has been discussed by Panagiotou *et al.* [21]. This step is necessary in order to properly distinguish between self-entanglements and entanglements between neighboring chains. Here, we provide a brief description of the scheme.

The periodic boundary condition needs to be removed in order to identify all entanglements properly. To understand the need for this step, consider a simple two-dimensional (2D) periodic box as shown in Fig. 7(a), containing just

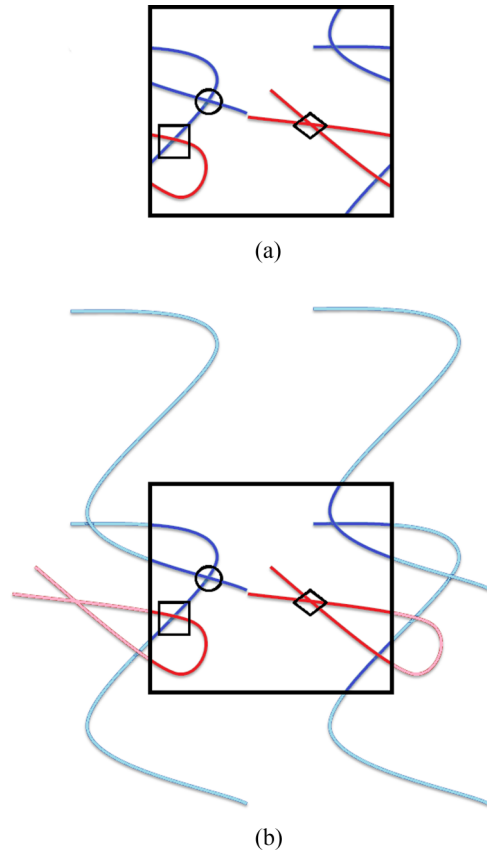


FIG. 7. (a) A 2D periodic box showing the periodic images of two chains shown in red and blue. Possible entanglements are marked by the circle, square, and diamond. The same entanglements are marked also in (b) where the chains are opened up across the boundaries. The circle and the square represent entanglements between two different chains, while the diamond encloses a self-entanglement.

two chains, the blue and the red. The small black circle encloses two segments of the blue chain, while the black square encloses a segment each of the red and the blue chains. The square encloses a potential entanglement between two different chains. However, the potential entanglement inside the circle is not necessarily a “self-entanglement” though the circle encloses two segments of the same blue chain. This becomes evident when we open up the periodic boundary condition (pbc) and complete all possible chains starting from the fragments inside the box in Fig. 7(b). Parts of chains inside the box are indicated by dark red or blue while parts that are obtained by opening up the periodic condition are denoted by lighter shades. Note from this figure that both the circled and squared crossings are potential entanglements between two separate chains. On the other hand, the possible entanglement enclosed with a diamond shape in Figs. 7(a) and 7(b) is indeed a self-entanglement. Opening up the periodic boundary condition and continuing all chains using their images inside the box allow us to properly identify entanglements between two chains and discount self-entanglements.

After removing the periodic boundary conditions, the following steps are performed to determine entanglements. Consider the situation shown in Fig. 8, where two neighboring chains are shown in blue and red:

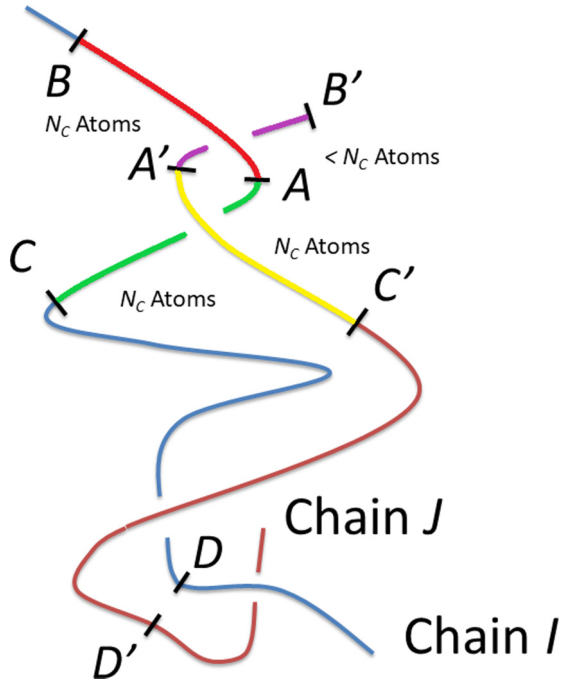


FIG. 8. Definition of quantities involved in calculating Lk_G between segments of two chains I and J .

(1) Identify the atoms A and A' on chains I and J that lie closest to each other.

(2) If the distance d between A and A' is less than d_c , a predetermined threshold distance, the segments around these two points can potentially be entangled. Otherwise, the red and blue chains are not close enough to be entangled. Most chain pairs do not form entanglements with each other. This step helps us discount the pairs that do not and identify the ones that do. In the present case, we have taken $d_c = 7 \text{ \AA}$, which is about twice the largest value of the LJ parameter σ .

(3) Calculate the linking number Lk_G between two segments BAC and $B' A' C'$, where BA , AC , $A' C'$ are all segments with N_c atoms each. Thus, in most cases, the linking number is determined for two neighboring open segments containing $2N_c$ atoms each. But, the segments may be shorter if the end of either chain is encountered (as in the case of the segment $A' B'$ on chain J). Equations (18) and (20) are used for the computation of Lk_G .

(4) If $|Lk_G|$ is more than L_c , the two segments are considered to be “entangled.” The end points of the two segments and the value of the linking number are stored. Arbitrarily, atom A on chain I and A' on J are taken to locate the topological entanglement points on these two chains.

The choice of the threshold L_c is somewhat arbitrary and based on our experience with the simple models shown in Fig. 6. In this work we have taken L_c to be 0.4, which implies that incomplete turns [as shown in Fig. 6(d)] of one segment about another also qualify as topological entanglements. As discussed in connection with Fig. 6(d), these can possibly disentangle in the course of deformation.

(5) We now leave the segments BAC and $B' A' C'$ out and search for the points (shown as D and D' in Fig. 8) which are

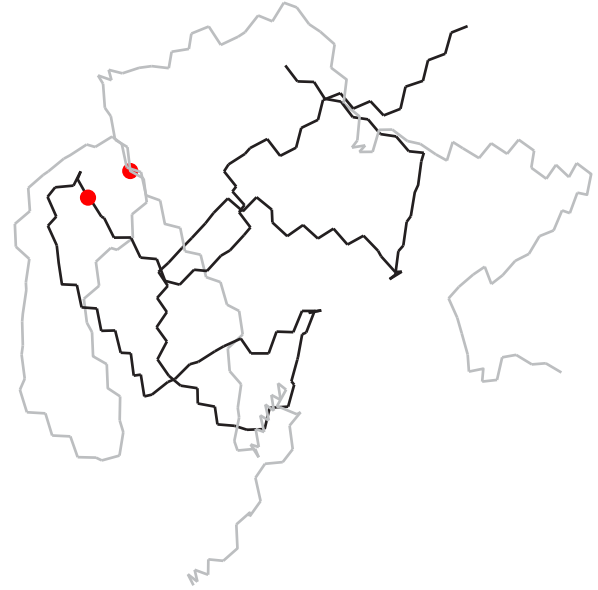


FIG. 9. A segment from one chain from the ensemble is entangled with a segment from a neighboring chain. The segments are shown in black and gray with the red circles marking the points on the chain which are taken to be the locations of the entanglement.

the closest in the rest of the two chains. The same steps are repeated for two segments centered at D and D' .

In the above scheme, the segment lengths used for the linking number calculation N_c need to be chosen. Our experience suggests that the algorithm is not sensitive to the exact value of N_c as long as it is of the order of the spacing between the entanglements. If the value is much smaller, we will end up performing many redundant calculations between segments that are not linked. If N_c is too large, entanglements that are located far apart along the two chains (and should be counted as independent) will get clubbed into one. We have heuristically chosen N_c to be a tenth of the chain length.

As described in Sec. II B and schematically shown in Fig. 2, we apply different deformation fields to the periodic box. The steps enumerated above are executed at regular intervals within the deformation history. We especially keep track of the location of entangling atom pairs and note the deformation level at which a particular pair disentangles.

A typical segment of a chain from the ensemble of 160 chains is shown in Fig. 9. The points marked in red are topological entanglement points. The light colored plot is of the corresponding segment of a neighboring chain with which the chosen chain is linked (for which $|Lk_G| > L_c$).

Comparison between methods based on PP analysis and Lk_G

Using the method outlined in the previous section, we are able to identify all segment pairs that have linking numbers greater than L_c . These are the topological entanglements and the topological entanglement length is the average number of united atoms between two consecutive topological entanglements along a chain.

As has been pointed out by several authors [9,13,15], the rheological entanglement length is typically larger than the topological entanglement length. What this means is that

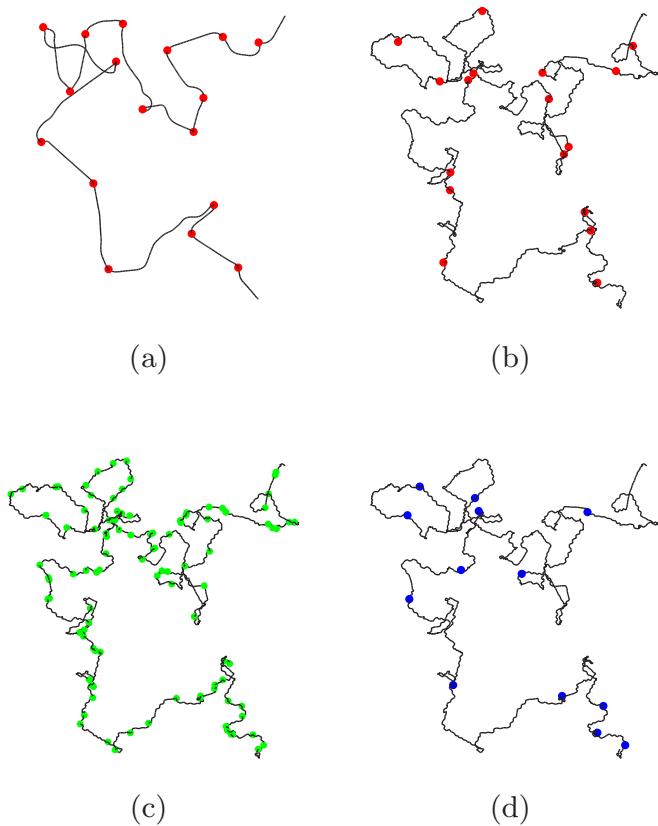


FIG. 10. The primitive path (PP) of the typical chain in (b) is shown in (a), with the kinks marked by solid red circles. The locations of the kinks are shown with solid circles on the actual chain in (b). Topological entanglements that satisfy $|Lk_G| > L_c$ are indicated for the same chain in (c). Rheological entanglement points obtained after optimized `kmeans` clustering are indicated by solid blue circles in (d).

several closely spaced topological entanglements serve to act as on rheological entanglement. The rheological entanglement length is the average distance between regions that have several closely spaced topological entanglements and collectively constrain the mobility of the chain.

To apply PP analysis (PPA) to our sample, we closely follow the procedure outlined in Mahajan *et al.* [9] and in Sec. I. When all the chains become almost piecewise linear curves with kinks occurring at the points where a chain is constrained by another chain, the topological entanglement length (i.e., the average number of monomers between two successive entanglements on a chain) can be obtained by calculating the average number of kinks per chain. This, as reported by Mahajan *et al.* [9] and also according to our computations, is around 20 for the force field chosen. Rheological estimators, on the other hand, yield values that are close to 80 at 400 K [13].

In Fig. 10(a), the configuration of a chain after it is cooled down to 10 K is shown. Sharp kinks (marked by solid red dots) occur at locations where the chain is restricted from crossing another chain. The location of these kinks is then transferred to the actual chain [see Fig. 10(b)], marking the location of the entanglements. For the entire sample, the average distance between kinks turns out to be 79 at 100 K,

which is the temperature from which the PPA was initiated. This is almost identical to the rheological entanglement length reported for this sample.

For the same chain and $L_c = 0.4$, the number of points that have $|Lk_G| > L_c$ are shown in Fig. 10(c). The points shown (recall that the exact location is somewhat arbitrary and assigned to the points of closest approach between two segments that have $L_c > 0.4$) constitute topological entanglement points. Physically, these are points around which two segments on two different chains wind around each other.

Note that many of the topological entanglement points are closely clustered. Each cluster acts as a rheological entanglement in unison. Therefore, to determine the rheological entanglement points from Fig. 10(c), an additional final step needs to be carried out. In this step, we use the `kmeans` algorithm [42] for clustering the topological entanglement points on each chain. Each rheological entanglement point is a cluster constituted of all topological entanglements contained in it. The coordinates of the green points along the chain shown in Fig. 10(c) are input to the `kmeans` command in MATLAB, to be divided among k_c clusters. The command yields the centroidal indices of each of the k_c clusters. The number of clusters k_c needs to be optimized (the optimum number of clusters is k_{opt}) for each chain so that we obtain the best possible grouping of the topological entanglements into rheological ones. Techniques for doing this are common in conventional cluster analysis. The elbow method [43] minimizes the total intracluster variation to determine the number of clusters k_{min} at which the total within-cluster sum of square (WSS) plotted against k_c shows an elbow. Now for each $k_c > k_{min}$, we determine the silhouette values [44] for every individual cluster. The silhouette value, which lies between -1 and 1 , is a measure of how well each point has been classified. The number of clusters k_c for which the variance in the silhouette values is the smallest is chosen as k_{opt} .

Every cluster of topological entanglement points serves as a rheological entanglement. Thus, for the chain in Fig. 10(c), after clustering, the rheological entanglement points are shown in blue solid circles in Fig. 10(d). Note that these points are assigned at the numeric center of the individual clusters and are not expected to match exactly with the kink locations in PPA. But, comparing with Fig. 10(b), we see that the location of the clusters is close to what PPA predicts for this chain. In fact, the average distance between clusters is 79, identical to the average distance between kinks in PPA.

The exercise of clustering the entanglement points has been done only to demonstrate that once we distinguish between topological and rheological entanglements, the entanglement distance obtained by our method closely matches that by PPA. In the subsequent sections, unless explicitly mentioned otherwise, “entanglements” will refer only to topological ones.

III. RESULTS AND DISCUSSION

Understanding the role of disentanglement of macromolecules during deformation and failure in the glassy state is an immediate and interesting application of the method of characterization that we outlined above. As discussed earlier, we have applied four deformation fields to our sample. Moreover, a disentanglement event is taken to occur at the moment

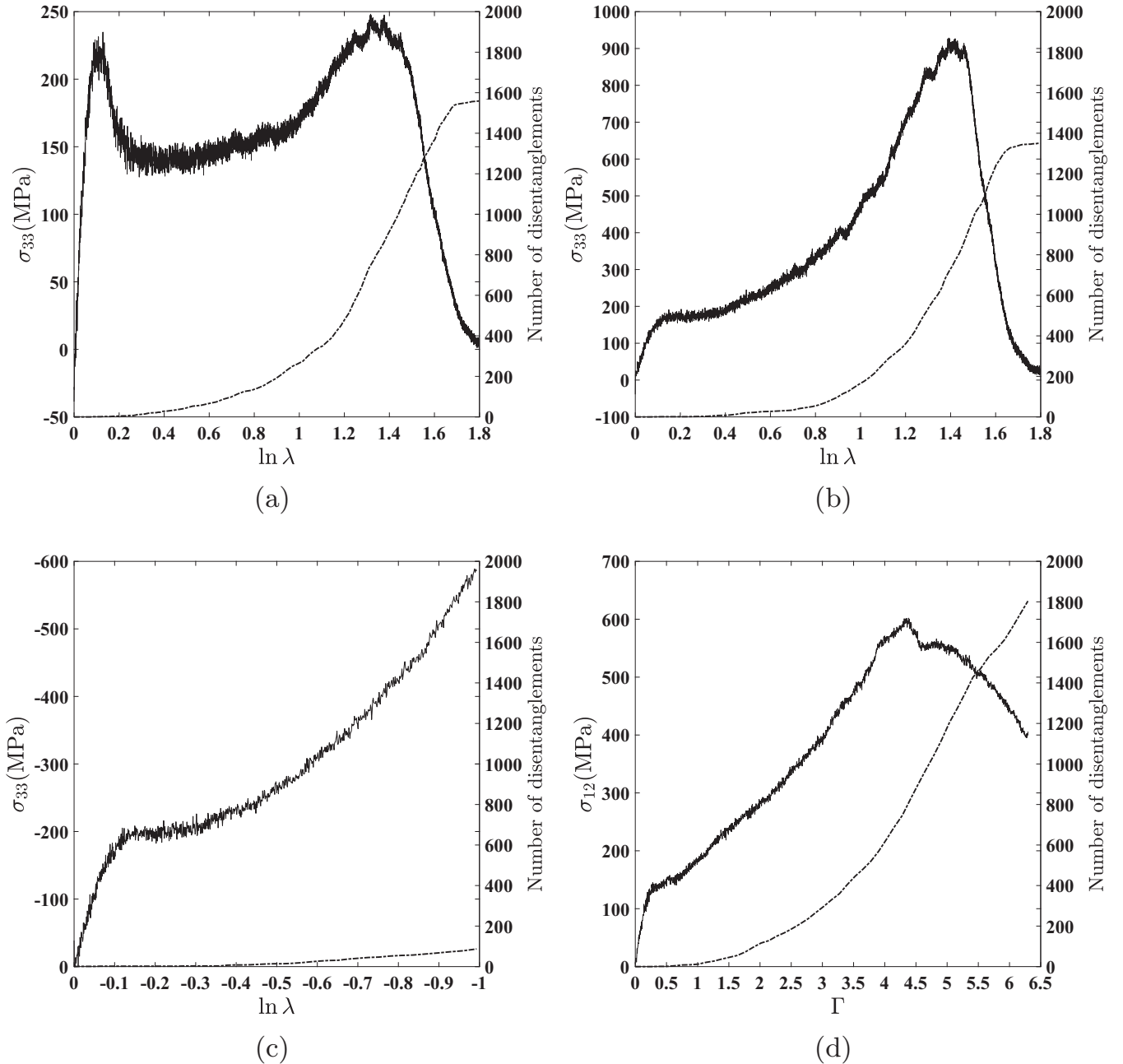


FIG. 11. The variations of stress component σ_{33} with $\ln \lambda$ are shown in (a) uniaxial stretch under high hydrostatic stress, (b) pure uniaxial stretch, and (c) pure compression. In (d), the variation of σ_{12} with Γ is shown. In all cases, the dashed curve indicates the number of disentanglement events during deformation.

when two chain segments with $|Lk_G| > L_c$ at $\lambda = 1$ ($\Gamma = 0$ for simple shear) has $|Lk_G| < L_c$ at some $\lambda > 1$ ($\Gamma > 0$ for simple shear).

With these definitions in place, we show that we can quantify deformation levels at which failure of the polymer through large scale disentanglement becomes possible in the glassy state. We demonstrate three important facts. First, large scale disentanglement is the primary cause of failure only in special states of deformation while other mechanisms like scission of chains should be responsible for failure in others. Second, severely limited mobility of chains in the glassy state requires that most disentanglement events are confined to entanglements that are located close to a chain end. Third,

it is possible to link the Gaussian linking number in the undeformed sample to the propensity to disentangle during deformation.

The normal stress response with $\log \lambda$ for the first three deformation fields is shown in Figs. 11(a)–11(c), while the variation of the shear stress σ_{12} with Γ is shown in Fig. 11(d). We do not have any mechanism of chain scission built into our simulation scheme and, therefore, the final failure can occur only with large scale disentanglement. The number of disentanglements occurring with deformation is also plotted in each of the figures.

For the case in Fig. 11(a), where a uniaxial stretch with an imposed hydrostatic state of stress has been applied, the

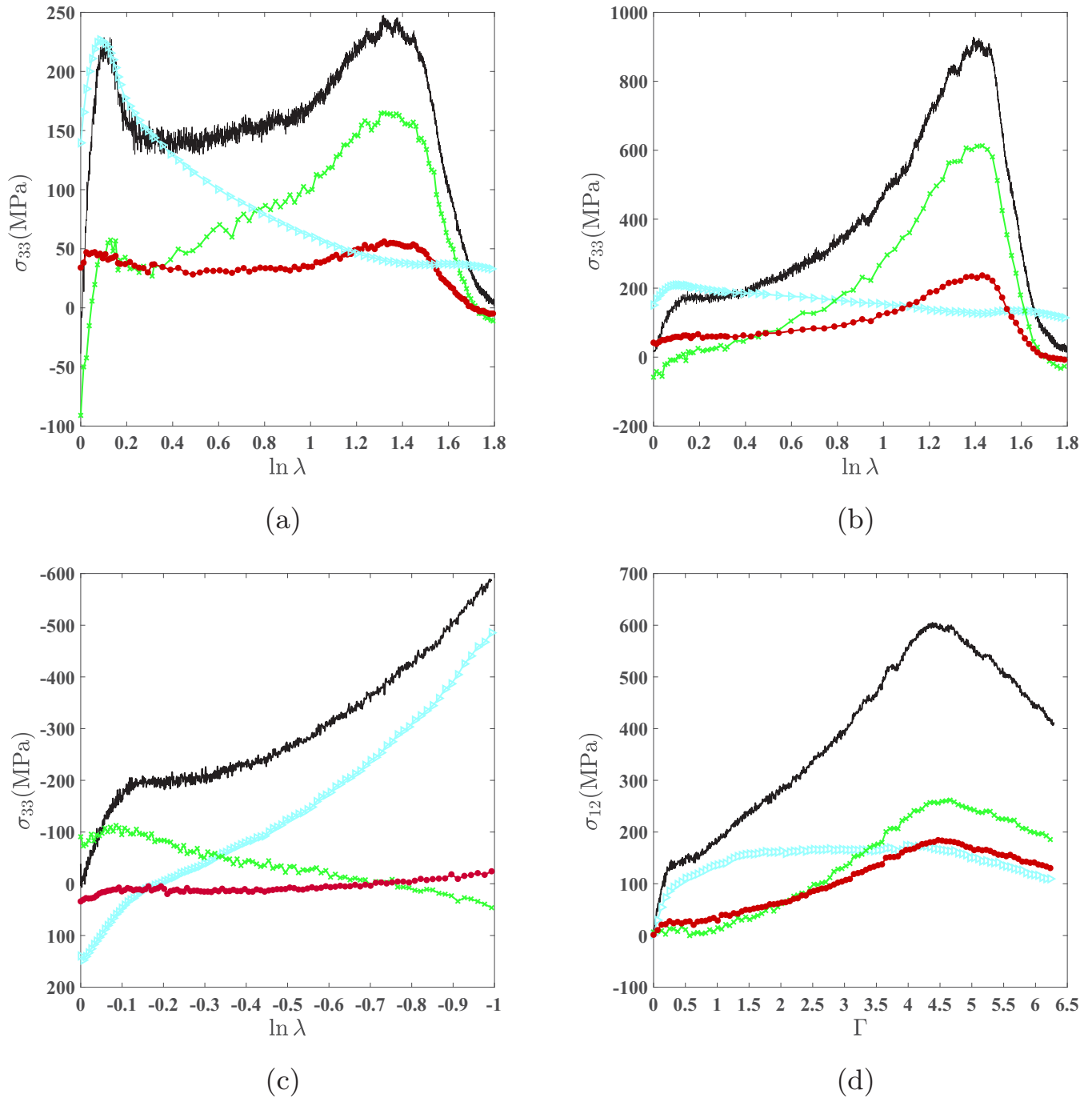


FIG. 12. Partitioning of total stress into contributions arising out of the nonbonded (blue), bonded (green), and torsion (red) parts of the force field for (a) uniaxial stretch under high hydrostatic stress, (b) pure uniaxial stretch, (c) pure compression, and (d) simple shear.

stress-stretch response represents that of a typical glassy polymer, with an elastic region followed by the “yield drop,” stress plateau, steep rehardening, and eventual rapid loss of stress carrying capacity leading to failure. Rapid disentanglement starts at large stretches toward the end of the stress plateau region and is the cause of the steep drop in stress carrying capacity. Disentanglements are very rare at small strains.

Figure 11(a) should be compared with Fig. 12(a), where the contributions to σ_{33} from the different constituents of the force field are plotted. At large strains, a significant part

of the total stress results from the nonbonded interactions. The rapid rise in the number of disentanglements as well as the rehardening and steep drop in the total stress carrying capacity coincides with a similar steep drop in the stress due to the LJ pair potential. In the case where the sample is uniaxially stretched with an imposed hydrostatic stress, disentanglement is closely correlated with the stress arising out of the nonbonded potential.

The situation in the case where the sample is subjected to a pure uniaxial stretch is shown in Figs. 11(b) and 12(b). Again, rapid disentanglement starts with rehardening. However, the

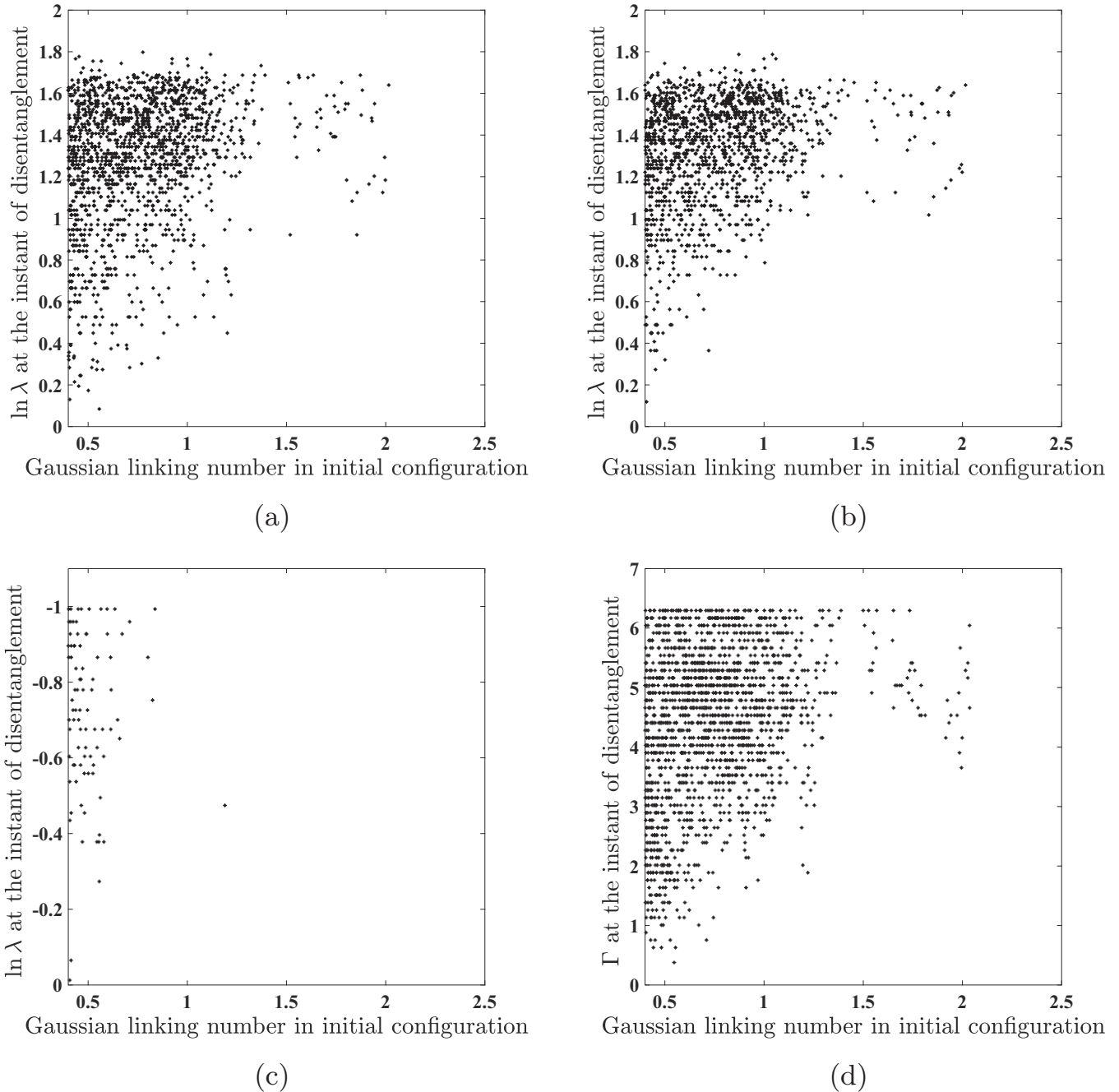


FIG. 13. Plots showing strains at which disentanglement events occur for a pair of segments with a particular Gaussian linking in the initial configuration for (a) uniaxial stretch under high hydrostatic stress, (b) pure uniaxial stretch, (c) pure compression, and (d) simple shear.

rehardening in this case [as seen from Fig. 12(b)] is due to stress carried by the bond stretch potentials rather than the nonbonded one. Since we do not account for bond scission in our simulations (see also [12]), in pure tension, bonds can get stretched by unrealistic extents leading to very large rise in stress carrying capacity. In reality, glassy polymers do not sustain such magnitudes of tensile stress as failure by bond scission intervenes much earlier. The situation depicted in Fig. 11(b), where failure by disentanglement eventually follows a steep rehardening, is somewhat artificial as chain scission is likely to be the dominant cause of failure in this case.

Figures 11(c) and 12(c) pertain to the case where the sample is subjected to uniaxial compression. Clearly, disentanglement is completely suppressed in uniaxial compression. The stress carrying capacity of the polymer at large strains is almost entirely due to nonbonded interactions. As disentanglement does not happen, the material does not fail. In the case where simple shear is imposed on the sample [Figs. 11(d) and 12(d)], hardening is due to bond stretching as in the case of pure uniaxial tension. Here too, disentanglement leads to a loss in stress carrying capacity because bond scission is suppressed. Rapid disentanglement and drop in stress carrying capacity sets in at unrealistically high values of Γ .

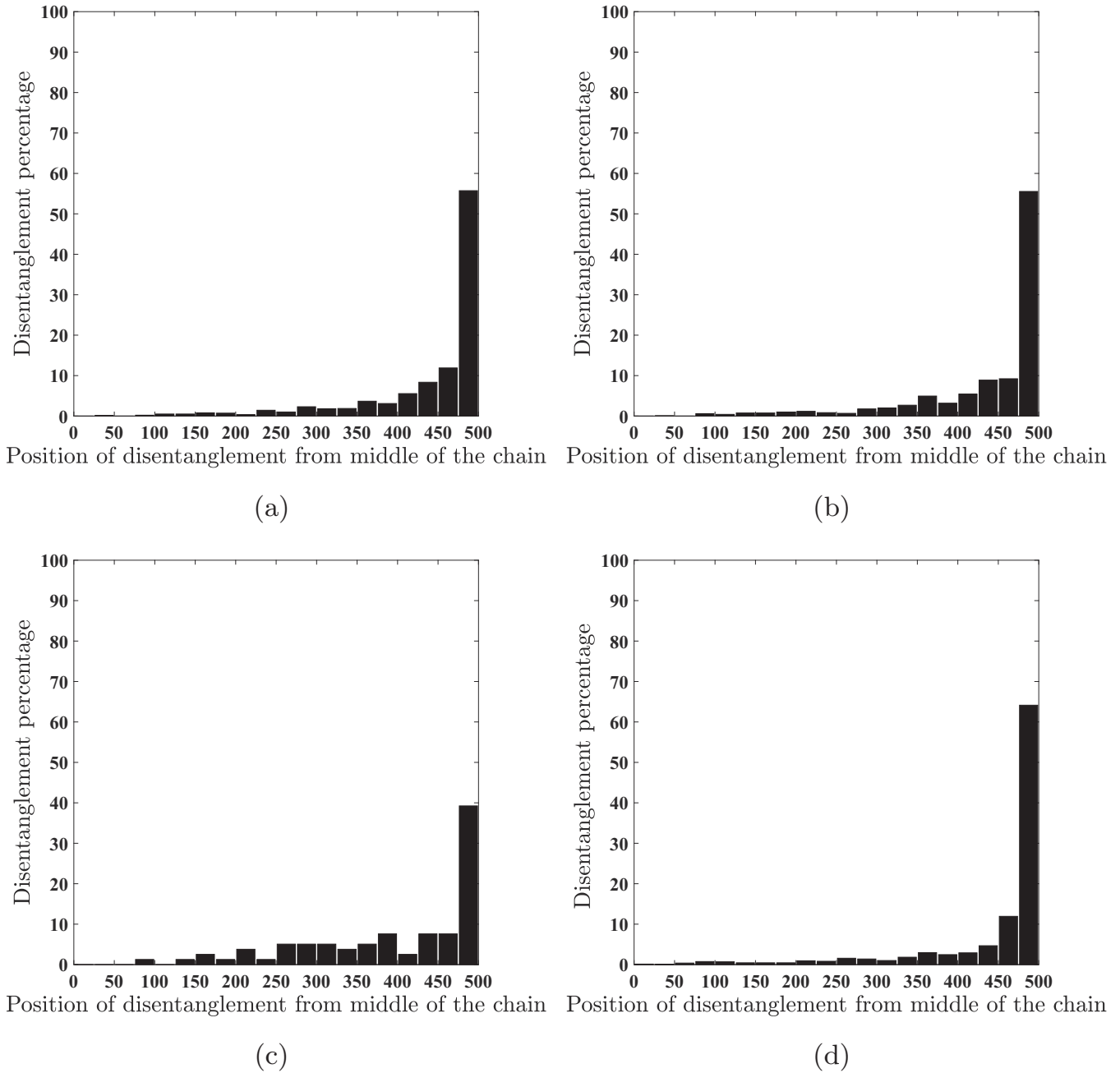


FIG. 14. Histograms the location from the center of a chain where disentanglements occur for (a) uniaxial stretch under high hydrostatic stress, (b) pure uniaxial stretch, (c) compression, and (d) simple shear.

Such high values will never be achieved in reality and bond scission will intervene to cause failure at much lower values of Γ .

It is clear from the above discussion that failure by disentanglement is the major cause of loss in stress carrying capacity only in the case where the material is uniaxially stretched with a superposed hydrostatic tension. Such a situation is typically achieved in polymers at regions of high stress triaxiality, e.g., near the tip of a sharp crack. In other modes of imposed deformation, disentanglement is either suppressed (as in uniaxial compression) or is expected to be preceded by chain scission (as in pure tension or simple shear).

The probability that an entanglement with $|Lk_G| > L_c$ at the onset of deformation will eventually disentangle also depends on the extent of deformation. In Figs. 13(a)–13(d), each disentanglement event is denoted by a point in the $\log \lambda$ (Γ for shear) versus $|Lk_G|$ plane for the four deformation fields used in this work. The Gaussian linking number can be thought of as an effective indicator of entanglement strength if entanglements that had high linking numbers at the start of deformation are seen to resist disentanglement until very large deformations. That this is indeed the case is seen from Figs. 13(a), 13(b), and 13(d), where all disentanglement events involving points with $Lk_G > 1.4$,

happen at deformation levels where the polymer has started to suffer loss in stress carrying capacity. The density of points in these plots indicates that while at low levels of deformation some sporadic disentanglement does occur in points with $Lk_G \simeq L_c$, the bulk of the disentanglement events occur later in the deformation history, close to failure. For compression [see Fig. 13(c)], very few disentanglement events happen and fail by rapid disentanglement does not occur.

From the simulations, it is also possible to track the locations at which disentanglement events happen. Since our samples comprise chains with 1000 monomers each, an entanglement located close to the end of the chain will be 500 monomers away from the middle. The number of disentanglement events as a function of the location of the entanglement point with respect to the middle of the chain is plotted in Figs. 14(a)–14(d). In all cases, almost all disentanglement events occur in cases where the entanglement point is located close to a chain end. Low levels of chain mobility in the glassy state require that the only possible mechanism of disentanglement is the one where a chain end slides out of a link. The number of chain ends is therefore expected to indirectly determine strength. Polydisperse polymers, with a large number of short chains, will have lower strength than monodisperse ones with the same average number of monomers per chain.

IV. CONCLUSIONS

A method for identifying and enumerating topological entanglements between two segments lying on closely located but different chains has been proposed. The method relies on a fast and reliable computation of the Gaussian linking number between the two segments. Topologically, an entanglement is identified as winding of a segment around another. Topological entanglement points are located wherever two chain segments exhibit linking numbers larger than a threshold value L_c . An additional step of optimally clustering such topological entanglement points leads to a reasonable measure of the rheological entanglement length.

Using the proposed method, it is possible to track every entanglement in a deforming ensemble of macromolecules. This is important as the eventual failure of a polymeric material often is caused by chain pullouts resulting from large scale disentanglement. We show that disentanglement is expected to be a major mechanism of failure in situations where the stress triaxiality is high. Also, the absolute value of the linking number is a good indicator of the survival probability of an entanglement under a imposed deformation field, i.e., entanglement points with larger linking numbers disentangle later in the deformation history. Finally, as the mobility of chains is very low in the glassy state, disentanglements overwhelmingly occur for entanglement points that are located close to a chain end.

-
- [1] D. Sumners and S. Whittington, Knots in self-avoiding walks, *J. Phys. A: Math. Gen.* **21**, 1689 (1988).
 - [2] K. Kremer and G. S. Grest, Dynamics of entangled linear polymer melts: A molecular-dynamics simulation, *J. Chem. Phys.* **92**, 5057 (1990).
 - [3] W. Graessley and S. Edwards, Entanglement interactions in polymers and the chain contour concentration, *Polymer* **22**, 1329 (1981).
 - [4] M. Doi and S. F. Edwards, *The Theory of Polymer Dynamics*, Vol. 73 (Oxford University Press, Oxford, 1988).
 - [5] M. C. Boyce, D. M. Parks, and A. S. Argon, Large inelastic deformation of glassy polymers. part i: Rate dependent constitutive model, *Mech. Mater.* **7**, 15 (1988).
 - [6] P. Wu and E. Van Der Giessen, On improved network models for rubber elasticity and their applications to orientation hardening in glassy polymers, *J. Mech. Phys. Solids* **41**, 427 (1993).
 - [7] Y. Tomita and S. Tanaka, Prediction of deformation behavior of glassy polymers based on molecular chain network model, *Int. J. Solids Struct.* **32**, 3423 (1995).
 - [8] L. Anand and M. E. Gurtin, A theory of amorphous solids undergoing large deformations, with application to polymeric glasses, *Int. J. Solids Struct.* **40**, 1465 (2003).
 - [9] D. K. Mahajan, B. Singh, and S. Basu, Void nucleation and disentanglement in glassy amorphous polymers, *Phys. Rev. E* **82**, 011803 (2010).
 - [10] S. Venkatesan and S. Basu, Investigations into crazing in glassy amorphous polymers through molecular dynamics simulations, *J. Mech. Phys. Solids* **77**, 123 (2015).
 - [11] D. K. Mahajan and S. Basu, On the simulation of uniaxial, compressive behavior of amorphous, glassy polymers with molecular dynamics, *Int. J. Appl. Mech.* **2**, 515 (2010).
 - [12] V. Sudarkodi, S. Basu *et al.*, Investigations into the origins of plastic flow and strain hardening in amorphous glassy polymers, *Int. J. Plast.* **56**, 139 (2014).
 - [13] R. S. Hoy, K. Foteinopoulou, and M. Kröger, Topological analysis of polymeric melts: Chain-length effects and fast-converging estimators for entanglement length, *Phys. Rev. E* **80**, 031803 (2009).
 - [14] S. K. Sukumaran, G. S. Grest, K. Kremer, and R. Everaers, Identifying the primitive path mesh in entangled polymer liquids, *J. Polym. Sci., Part B: Polym. Phys.* **43**, 917 (2005).
 - [15] C. Tzoumanekas and D. N. Theodorou, Topological analysis of linear polymer melts: A statistical approach, *Macromolecules* **39**, 4592 (2006).
 - [16] M. Kröger, Shortest multiple disconnected path for the analysis of entanglements in two- and three-dimensional polymeric systems, *Comput. Phys. Commun.* **168**, 209 (2005).
 - [17] S. Shanbhag and R. G. Larson, Identification of topological constraints in entangled polymer melts using the bond-fluctuation model, *Macromolecules* **39**, 2413 (2006).
 - [18] K. Foteinopoulou, N. C. Karayiannis, V. G. Mavrantzas, and M. Kröger, Primitive path identification and entanglement statistics in polymer melts: Results from direct topological analysis on atomistic polyethylene models, *Macromolecules* **39**, 4207 (2006).
 - [19] K. C. Millett, Knotting and linking in macromolecules, <http://web.math.ucsb.edu/~millett/Papers/Millett2018Tokyoreport1.5.pdf>.

- [20] Y. Kantor, Knots in polymers, *Pramana: J. Phys.* **64**, 1011 (2011).
- [21] E. Panagiotou, C. Tzoumanekas, S. Lambropoulou, K. C. Millett, and D. N. Theodorou, A study of the entanglement in systems with periodic boundary conditions, *Prog. Theor. Phys.* **191**, 172 (2011).
- [22] E. Panagiotou, M. Kröger, and K. C. Millett, Writhe and mutual entanglement combine to give the entanglement length, *Phys. Rev. E* **88**, 062604 (2013).
- [23] E. Panagiotou, K. C. Millett, and P. J. Atzbereger, Topological methods for polymeric materials: Characterizing the relationship between polymer entanglement and viscoelasticity, *Polymers* **11**, 437 (2019).
- [24] J. Qin and S. T. Milner, Counting polymer knots to find the entanglement length, *Soft Matter* **7**, 10676 (2011).
- [25] F. Ferrari, J. Paturej, M. Piatek, and Y. Zhao, Knots, links, anyones and statistical mechanics of entangled polymer rings, *Nucl. Phys. B* **945**, 114673 (2019).
- [26] L. Tubiana, E. Orlandini, and C. Micheletti, Probing the entanglement and locating knots in ring polymers: A comparative study of different arc closure schemes, *Prog. Theor. Phys. Supplement* **191**, 192 (2011).
- [27] H. L. Frisch and E. Wasserman, Chemical topology, *J. Am. Chem. Soc.* **83**, 3789 (1961).
- [28] M. Delbrück, Knotting problems in biology, in *Proceedings of Symposia in Applied Mathematics*, Vol. 14 (American Mathematical Society, Providence, RI, 1962), pp. 55–63.
- [29] E. Panagiotou, K. C. Millett, and S. Lambropoulou, The linking number and the writhe of uniform random walks and polygons in confined spaces, *J. Phys. A: Math. Theor.* **43**, 045208 (2010).
- [30] M. L. Mansfield, Are there knots in proteins? *Nat. Struct. Biol.* **1**, 213 (1994).
- [31] E. Orlandini, M. Tesi, and S. Whittington, Polymer entanglement in melts, *J. Phys. A: Math. Gen.* **33**, L181 (2000).
- [32] M. Caraglio, C. Micheletti, and E. Orlandini, Physical links: defining and detecting inter-chain entanglement, *Sci. Rep.* **7**, 1156 (2017).
- [33] K. Klenin and J. Langowski, Computation of writhe in modeling of supercoiled DNA, *Biopolymers* **54**, 307 (2000).
- [34] M. Fukuda and S. Kuwajima, Molecular dynamics simulation of water diffusion in atactic and amorphous isotactic polypropylene, *J. Chem. Phys.* **108**, 3001 (1998).
- [35] S. Plimpton, Fast parallel algorithms for short-range molecular dynamics, *J. Comput. Phys.* **117**, 1 (1995).
- [36] A. P. Thompson, S. J. Plimpton, and W. Mattson, General formulation of pressure and stress tensor for arbitrary many-body interaction potentials under periodic boundary conditions, *J. Chem. Phys.* **131**, 154107 (2009).
- [37] N. C. Admal and E. B. Tadmor, A unified interpretation of stress in molecular systems, *J. Elast.* **100**, 63 (2010).
- [38] C. F. Gauss, *Werke: Fünfter Band* (Springer, Berlin, 1877), Chap. 42, pp. 601–630.
- [39] C. Nash, in *History of Topology*, edited by I. M. James (North-Holland, Amsterdam, 1999), Chap. 12, pp. 359–415.
- [40] Z. Arai, A rigorous numerical algorithm for computing the linking number of links, *Nonlinear Theory and Its Applications, IEICE* **4**, 104 (2013).
- [41] A. Van Oosterom and J. Strackee, The solid angle of a plane triangle, *IEEE Trans. Biomed. Eng.* **BME-30**, 125 (1983).
- [42] S. Lloyd, Least squares quantization in pcm, *IEEE Trans. Inf. Theory* **28**, 129 (1982).
- [43] D. J. Ketchen and C. L. Shook, The application of cluster analysis in strategic management research: an analysis and critique, *Strategic Manage. J.* **17**, 441 (1996).
- [44] P. J. Rousseeuw, Silhouettes: A graphical aid to the interpretation and validation of cluster analysis, *J. Comput. Appl. Math.* **20**, 53 (1987).